Additional File 1. Supplementary Figures and Legends

Figure S1. Adult Anopheles stephensi salivary gland lobe and cellular morphometry. (A) Graph of average length (blue) and width (red) of each lobe from *An. stephensi*. Ten samples were measured per lobe. Results indicate that lobe length varies more than lobe width, but variations are similar across lobes (standard deviations are shown on the graph). (B) Graph of adult *An. stephensi* SG cellular morphometry. Each data point represents 50 cellular measurements among 10 lobes. Results show low variability in both female and male gland cellular dimensions, except for proximal lateral cell length, which varies with asymmetric positioning of the duct within that part of the gland. (C) Cross-sections from Nile Red and DAPI stained SGs illustrating the number of nuclei in circumference in the female distal lateral (DL), proximal lateral (PL), and medial lobe (M), and male gland. Proximal (P) and distal (D) are labeled on each lobe/gland for orientation. Arrow in (PL) marks the PL cross-section. The number of circumferential nuclei varies along the length of each lobe. These cell shape and duct observations agree well with previously published electron microscopy cross-sectional views [11]. Scale bars are 50 microns long.

Figure S2. Additional details regarding adult *Drosophila* salivary gland cellular architecture. Adult *D. melanogaster* (Canton S) SGs stained with DAPI (nuclei), phalloidin (actin), and WGA (chitin; A) or Nile Red (lipids; B-D). A) Evidence of cell turnover was observed, including DNA fragmentation (white arrow), basal cell detachment, and actin accumulation (yellow arrow). (B-D) Female (B) and Male (C-D) SG cell shape. Results show Nile Red staining throughout the cell membranes, highlighting the cuboidal shape of the

secretory cells (e.g. Bii, white arrows). Actin is well organized into apico-basal fibers (Biii), and debris can sometimes be visualized in the lumen (Biv, white arrow). The lumenal surface appears irregular [compare Cii to D (proximal portion from another gland)]. Images not labeled with "MIP" (maximum intensity projections), are single slices. D is a MIP of two slices. Scale bar lengths are: 50 microns – A, Bi, Ci; 20 microns – Bii, Biii, Biv, Cii, D.

Figure S3. Larval *Drosophila* salivary gland nuclear dimension correlate with known ploidy. (A) Male *D. melanogaster* (Oregon R) larval SGs stained with DAPI (nuclei). Three classes of nuclei are visible: 1) imaginal nuclei (blue arrow), 2) duct nuclei (red arrow), and 3) secretory nuclei (green arrow). Imaginal nuclei are known to be diploid; duct nuclei are weakly polyploid and secretory nuclei are very highly polyploid (polytene). (B) Graph of nuclear diameters of these three cell types. Sample size is given at the base of each bar. Note that nuclear size increases with an increase in ploidy. (C) *An. stephensi* nuclear diameter measurements. A graph (Ci) of nuclear diameter measurements from two populations of cells (duct, and secretory cells), reveals that both cell types had consistently sized nuclei; secretory cell nuclei are a little more than twice the diameter of duct nuclei. Secretory cell and duct cell measurements were taken from Fig. 2A and similar images. Small DAPI body (micronucleus) measurements were taken from Cii. In this female DL lobe, micronuclei are abundant (sites of enriched DAPI and Nile Red colocalization). Micronucleus morphology was often elongated, not spherical, so maximal length was measured. Micronucleus length distribution is plotted in Ciii, sorted from smallest to largest. Discontinuous outlier values are boxed. (D) Visual comparison of *D. melanogaster* imaginal cell (Di) and *An. stephensi* micronucleus (Dii) size. Images are the same

scale, and nuclei of interest are marked by white arrows. *: p-value < 0.001 by pair-wise Mann-Whitney U tests. Scale bar lengths are: 50 microns – A, Dii; 20 microns – Ci, Cii.

Figure S4. Controls for fluorescence microscopy in *Anopheles stephensi* salivary glands. A-B) Consistency in immunofluorescence results when performed on frozen versus freshly dissected *An. stephensi* SG tissue. Shown are maximum intensity projections from either freshly dissected (A) or frozen, then thawed (B) adult female and male *An. stephensi* SGs stained with DAPI and Rh-WGA (chitin, O-GlcNAc groups). Similar staining effectiveness was observed on both tissue preparations. C) Secondary antibody background signal controls. Shown are maximum intensity projections from adult *An. stephensi* female or male SGs stained without adding primary antibody. When rabbit secondary antibodies were used in the absence of primary antibody, we detected weak duct staining and punctate cellular staining. This background signal disappeared in the presence of primary antisera against a variety of proteins (See Methods). Mouse secondary antibodies alone showed very little signal accumulation. Scale bars are 50 microns in length.

Figure S5. Conservation of the mosquito protein AAPP. A) Multiple sequence alignment of AAPP homologs from multiple mosquito species. Green: identical residue in all proteins. Yellow: conserved residue. Teal: similar residue. B) AAPP protein conservation tree diagram. AAPP is conserved within mosquitoes, but is not present in *Drosophila*. See Methods for additional details.

Figure S6. Conservation of the microtubule component protein α-tubulin. Multiple sequence alignment of α-tubulin homologs in mosquitoes and *Drosophila*. Green: identical residue in all proteins. Yellow: conserved residue. Teal: similar residue.

Figure S7. Conservation of the cis-Golgi-associated protein GM130. Multiple sequence alignment of GM130 homologs in mosquitoes and *Drosophila*. Green: identical residue in all proteins. Yellow: conserved residue. Teal: similar residue.

Figure S8. Conservation of the ER-associated KDEL receptor. Multiple sequence alignment of KDEL receptor homologs in mosquitoes and *Drosophila*. Green: identical residue in all proteins. Yellow: conserved residue. Teal: similar residue.

Figure S9. Conservation of the mitochondrial transcription factor mtTFA. Multiple sequence alignment of mtTFA homologs in mosquitoes and *Drosophila*. Green: identical residue in all proteins. Yellow: conserved residue. Teal: similar residue.

Figure S10. Conservation of the mosquito protein SG6. A) Multiple sequence alignment of SG6 homologs in several mosquito species. Green: identical residue in all proteins. Yellow: conserved residue. Teal: similar residue. B) SG6 protein conservation tree diagram. SG6 is conserved within mosquitoes, but is not present in *Drosophila*. See Methods for additional details.

Figure S1

A.

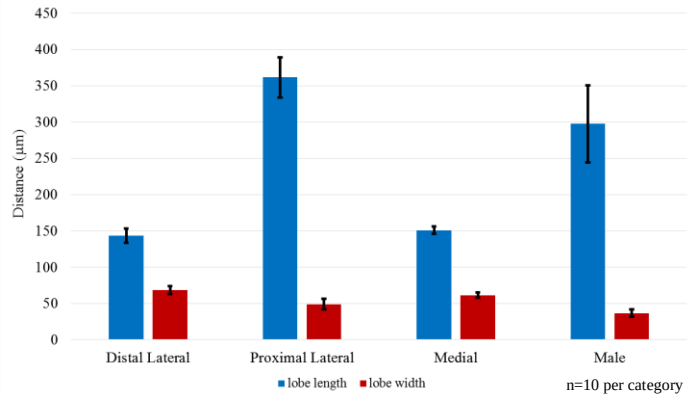

B.

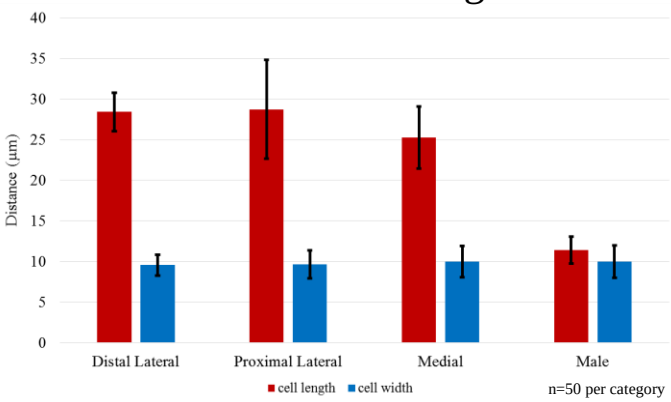

C.

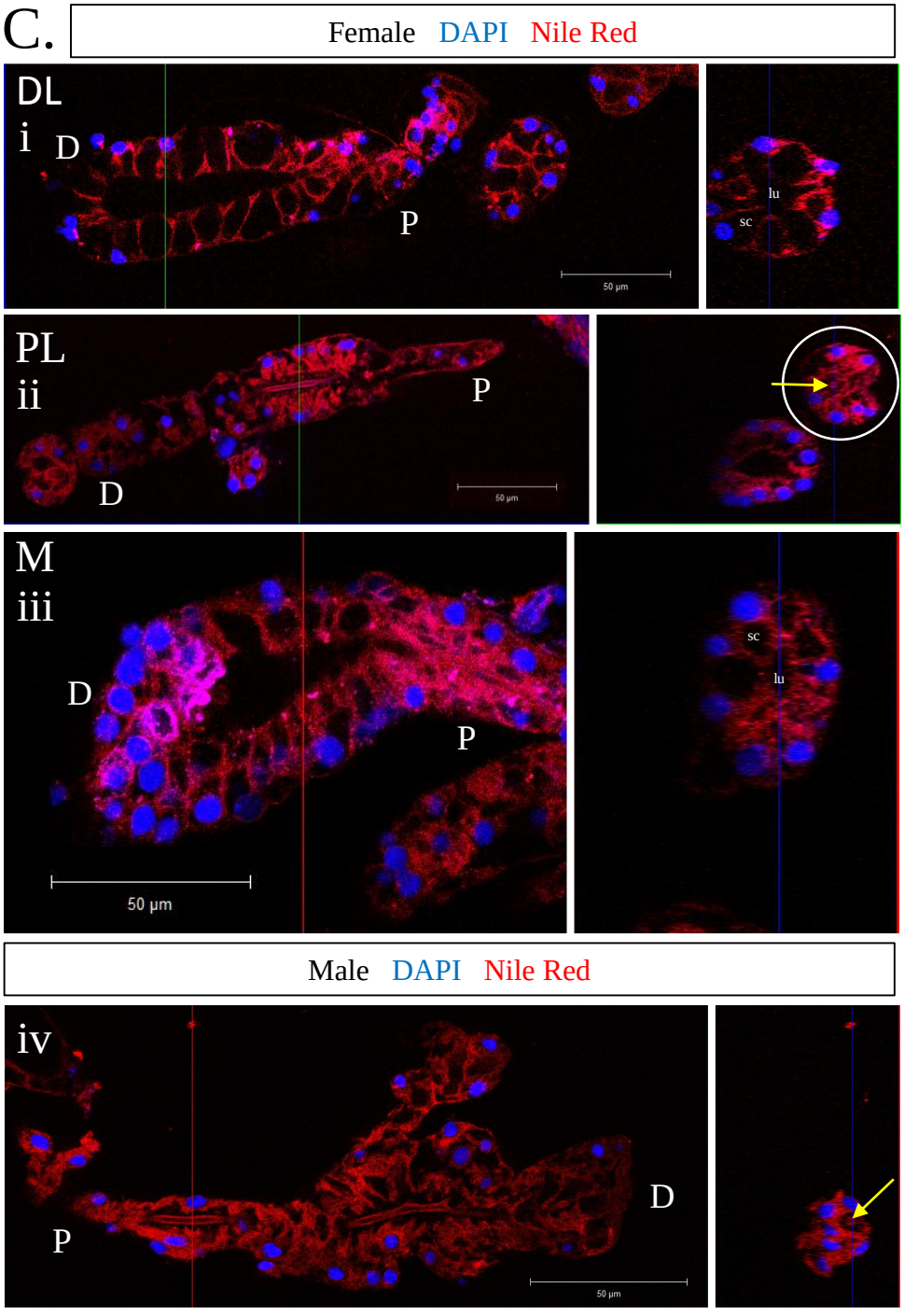

Figure S2

A.

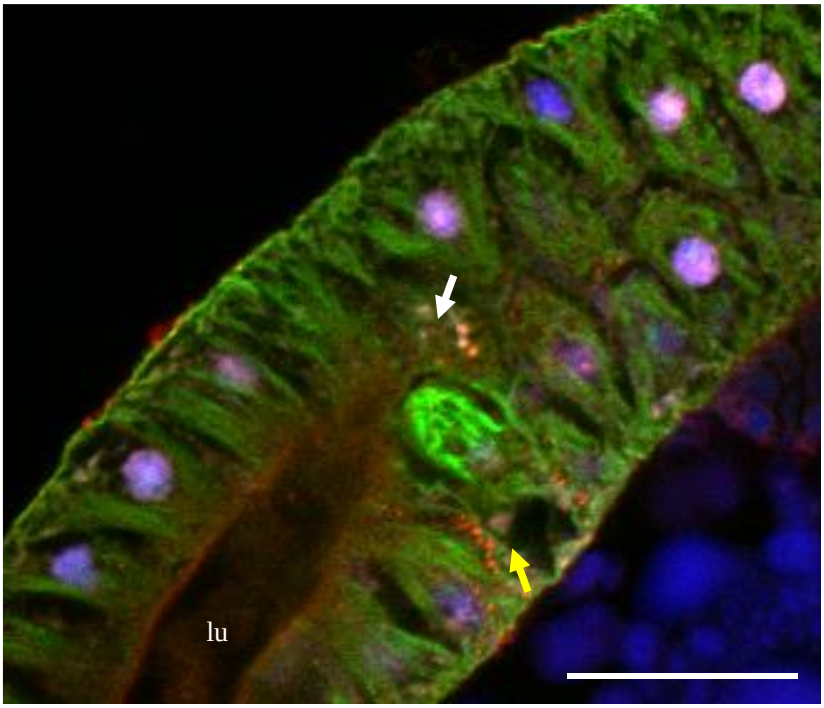

B.

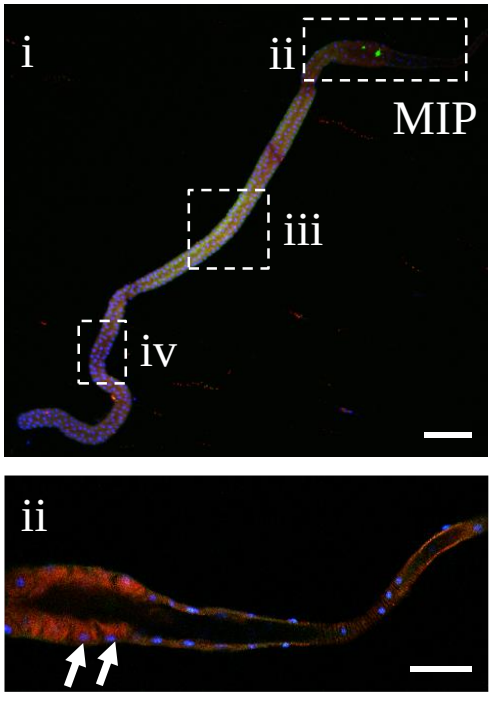

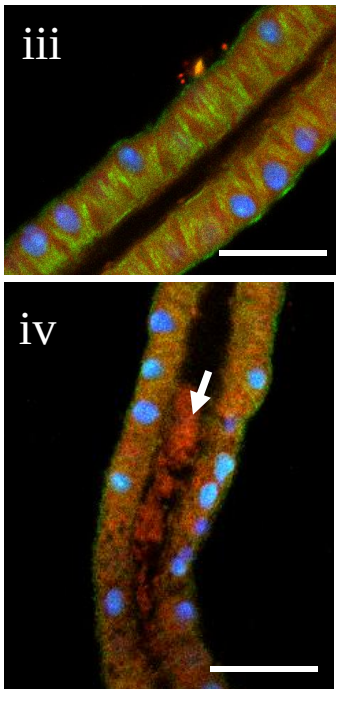

C.

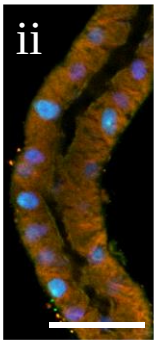

D.

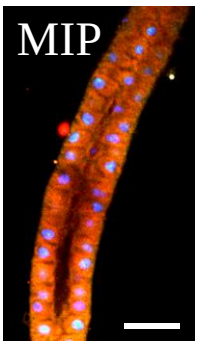

Figure S3

A.

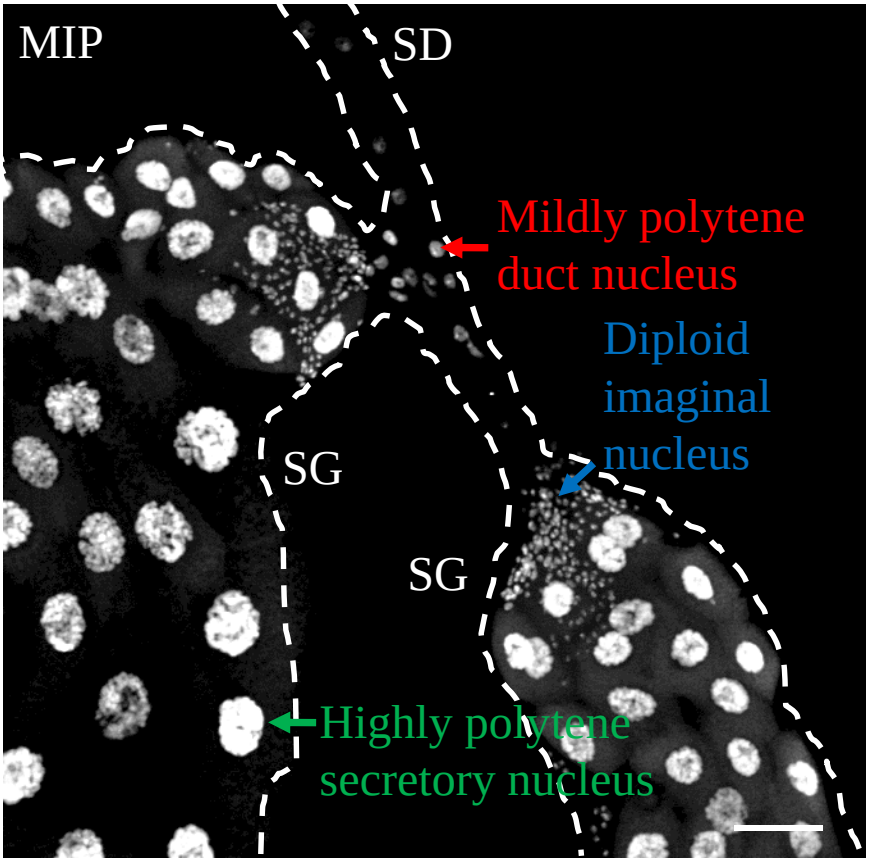

B.

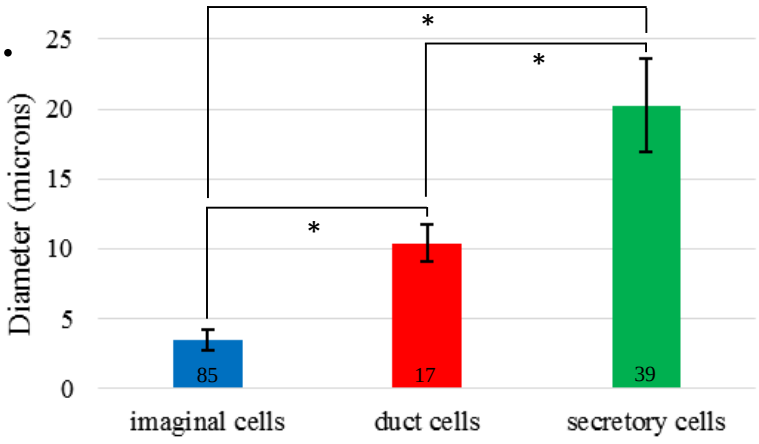

C. i

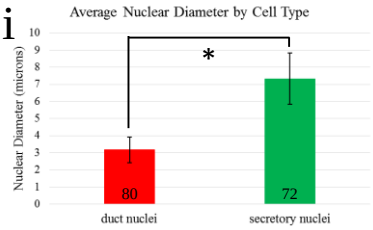

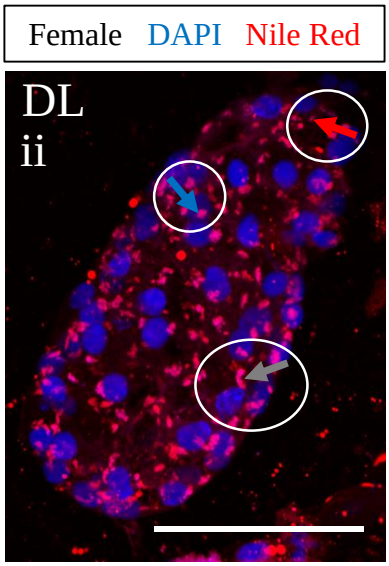

iii

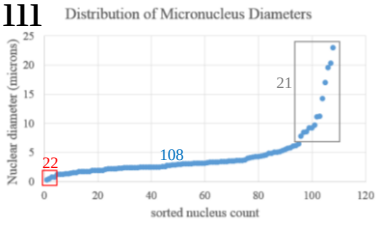

D.

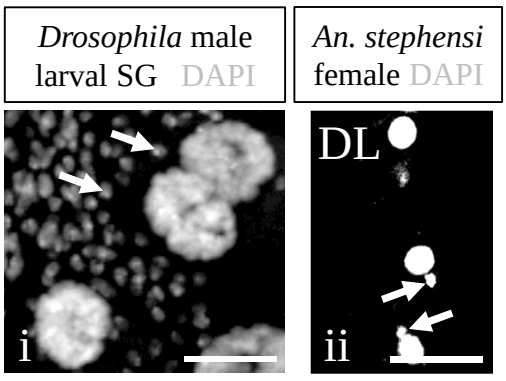

Figure S4

A.

Female DAPI WGA

FRESH

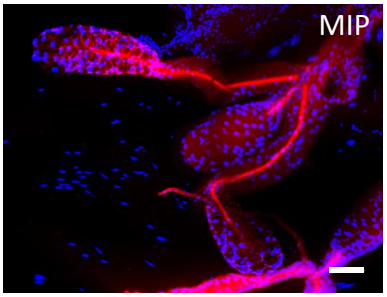

FROZEN

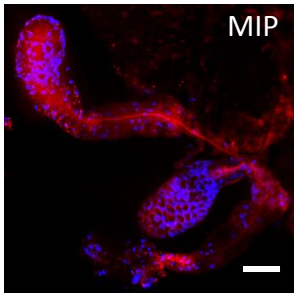

B.

Male DAPI WGA

FRESH

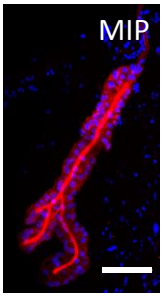

FROZEN

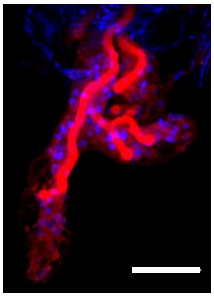

C.

DAPI Alexa 488 (rabbit)
Alexa 647 (mouse)

Female

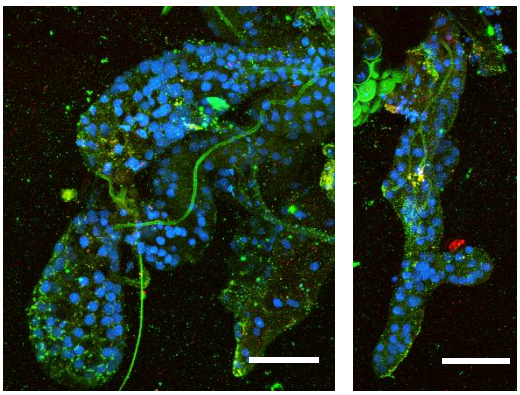

Figure S5

A.

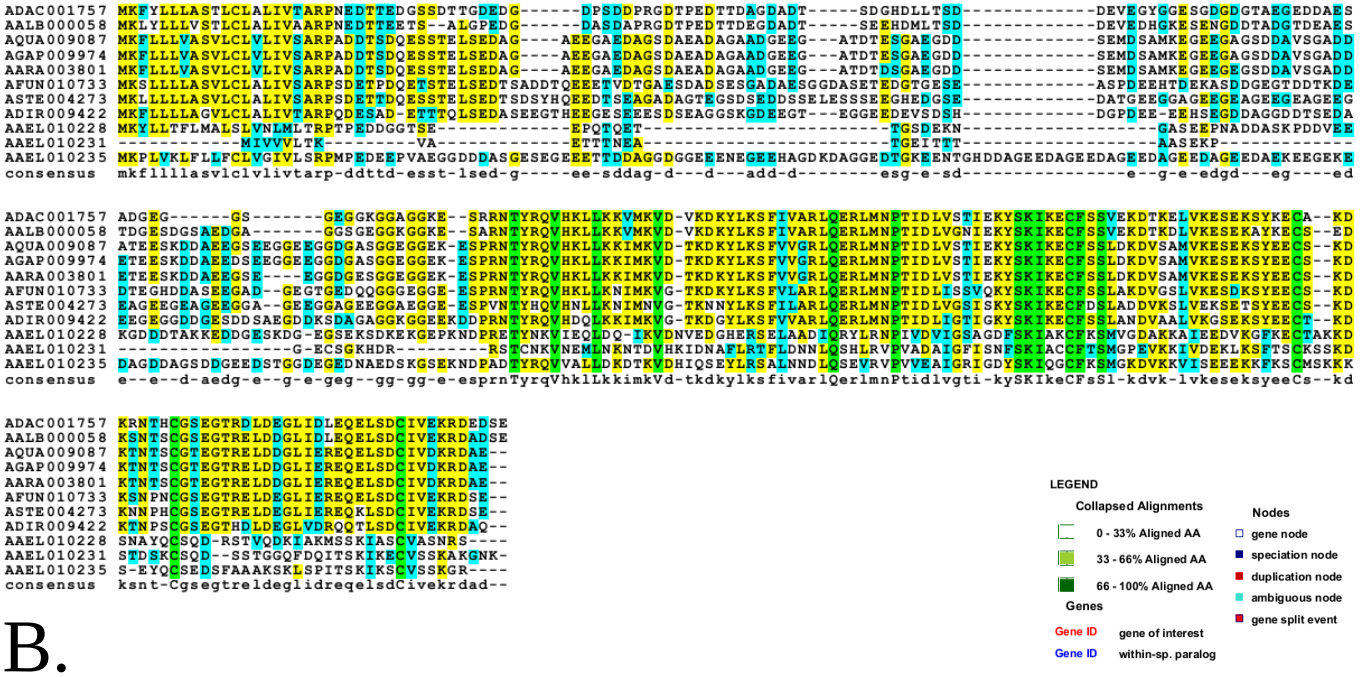
ADAC001757
AALB000058
AQUA009087
AGAP009974
AARA003801
AFUN010733
ASTE004273
ADIR009422
AAEL010228
AAEL010231
AAEL010235
consensus

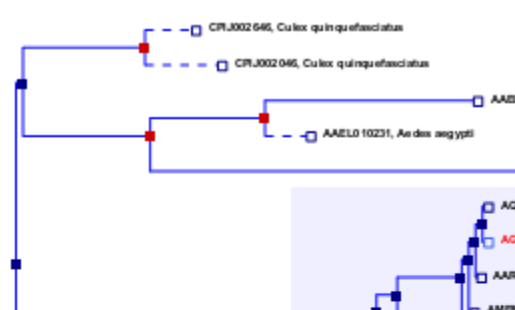
ADAC001757
AALB000058
AQUA009087
AGAP009974
AARA003801
AFUN010733
ASTE004273
ADIR009422
AAEL010228
AAEL010231
AAEL010235
consensus

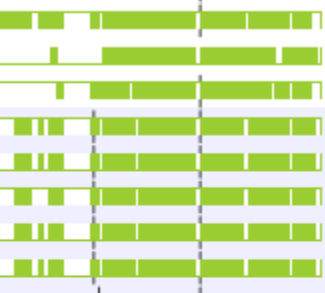
LEGEND
Collapsed Alignments
0 - 33% Aligned AA
33 - 66% Aligned AA
66 - 100% Aligned AA
Genes
Gene ID gene of interest
Gene ID within-sp. paralog
Nodes
gene node
speciation node
duplication node
ambiguous node
gene split event

B.

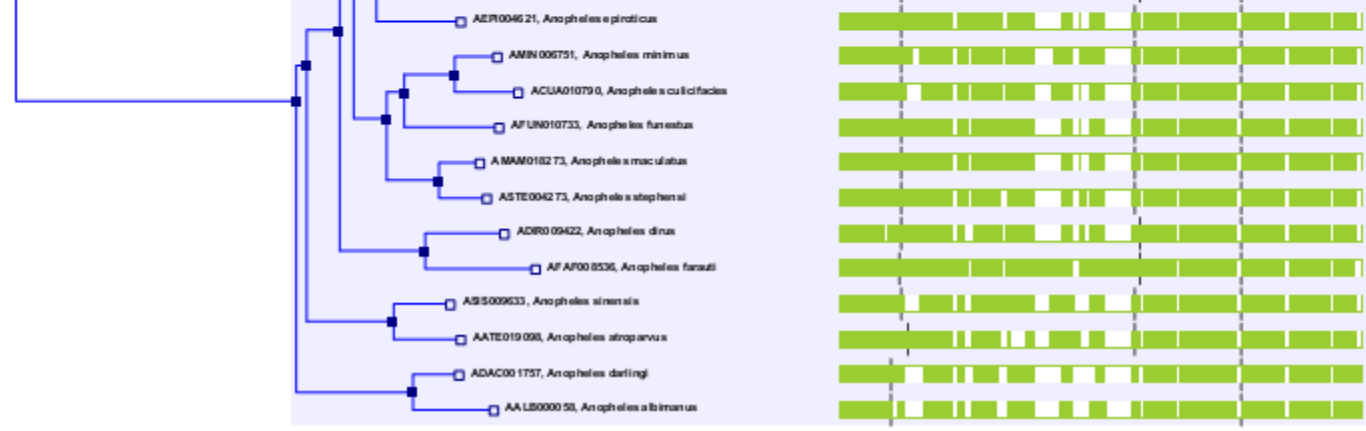
CPIJ002646, Culex quinquefasciatus
CPIJ002046, Culex quinquefasciatus
AAEL010235, Aedes aegypti
AAEL010231, Aedes aegypti
AAEL010228, Aedes aegypti
AQUA009087, Anopheles quadriannulatus
AGAP009974, Anopheles gambiae
AARA003801, Anopheles arabiensis
AMEM017930, Anopheles merus
AMEC010268, Anopheles melas
ACHR006324, Anopheles christyi
AEPI004621, Anopheles epiroticus
AMIN006751, Anopheles minimus
ACUA010790, Anopheles culicifacies
AFUN010733, Anopheles funestus
AMAM018273, Anopheles maculatus
ASTE004273, Anopheles stephensi
ADIR009422, Anopheles dirus
AFAF008536, Anopheles farauti
ASIS009633, Anopheles sinensis
AATE019098, Anopheles atroparvus
ADAC001757, Anopheles darlingi
AALB000058, Anopheles albimanus

Figure S6

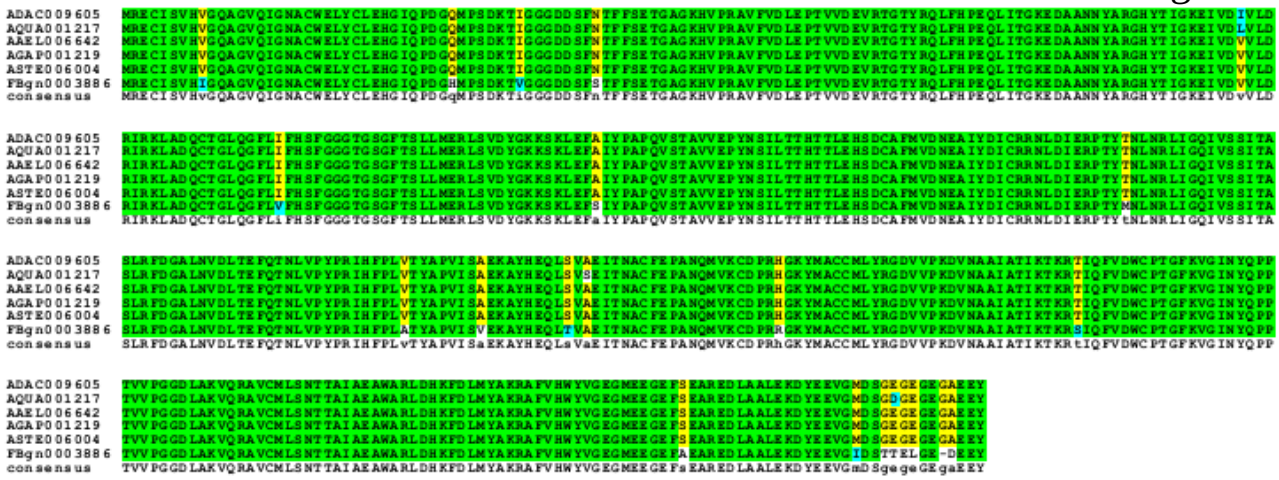
ADAC009605
AQUA001217
AAEL006642
AGAP001219
ASTE006004
FBgn0003886
consensus

Figure S7

Figure S8

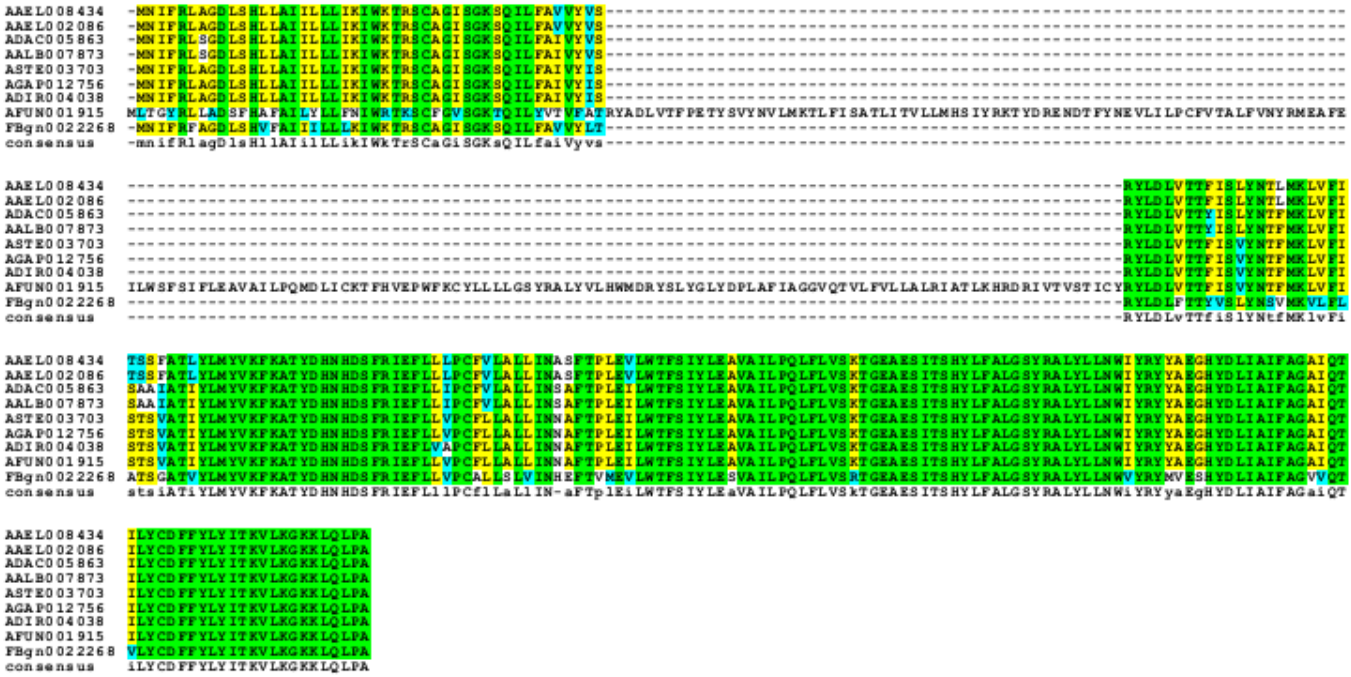
AAEL008434
AAEL002086
ADAC005863
AALB007873
ASTE003703
AGAP012756
ADIR004038
AFUN001915
FBgn0022268
consensus

Figure S9

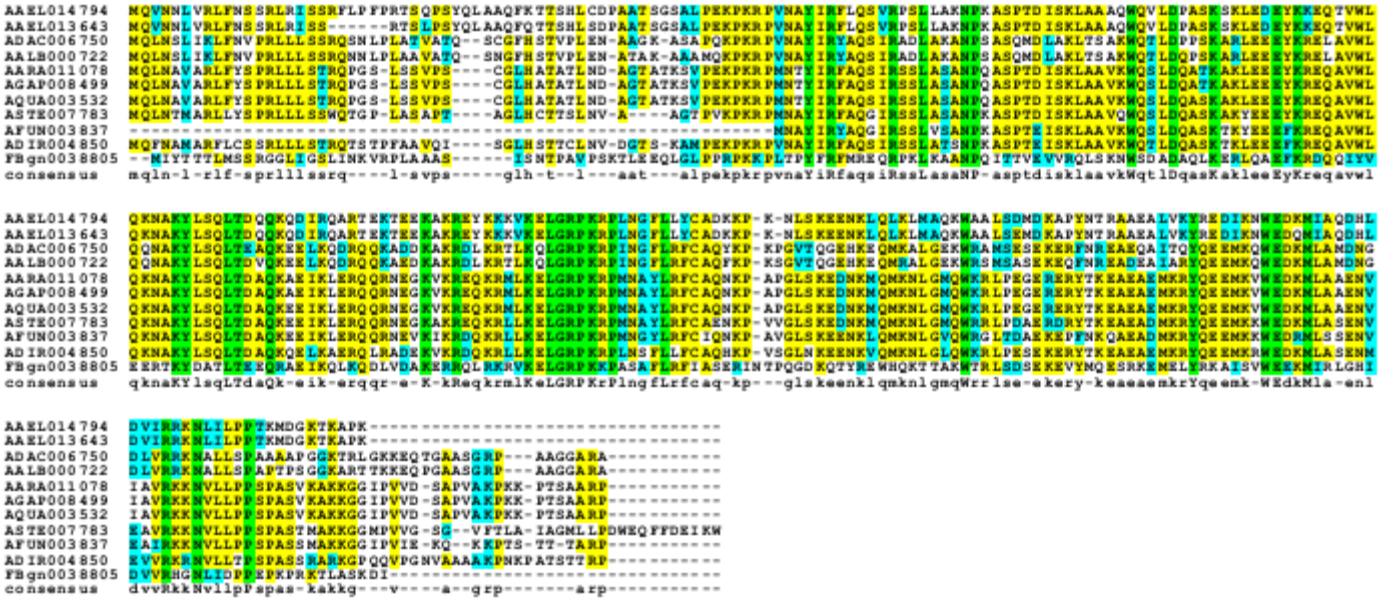
AAEL014794
AAEL013643
ADAC006750
AALB000722
AARA011078
AGAP008499
AQUA003532
ASTE007783
AFUN003837
ADIR004850
FBgn0038805
consensus

Figure S10

A.

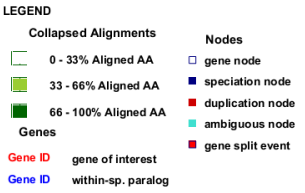

B.